Vol.3, No.6, Page 1408- 1418, 2025 https://doi.org/10.59628/jast.v3i6.1876 ISSN 2958-9568 JAST

SUN PUBLISHER

مجلة جامعة صنعاء للعلوم التطبيقية والتكنولوجيا

Sana'a University Journal of Applied Sciences and Technology

https://journals.su.edu.ye/index.php/jast/

Morphological and Optical Analysis of $\alpha - Al_2O_3 : Zn$ Nanoparticles

Eman Mohammed Ali Nassar[1]*, A.H. AL-Hammadi[1] and Yasser Hussein Issa Mohammed[2]

[1]**Department of Physics, Faculty of Science, Sana'a University, Sana'a, Yemen,**
[2]**Department of Pharmacy, Faculty of Medicine and Health Science, Hajjah University, Hajjah, Yemen**

*Corresponding author: e.nassar@su.edu.ye

Abstract

This study investigates the morphology and optical properties of prepared α-Al_2O_3:Zn nanoparticles by sol-gel method at room temperature. TEM image revealed hexagonal structure and the average particle size in the range (9.52-15.94 **nm**), and showed the particles distribution and area by histograms distribution. The Selected Area Electron Diffraction (SAED) illustrated the polycrystalline structure. XRD analysis confirmed hexagonal structure with a high crystalline and polycrystalline structure of α-Al_2O_3:Zn nanoparticles, the average crystallite size in the range (30.529- 24.057 **nm**). The optical study found that the energy gab of prepared α-Al_2O_3:Zn (0%, 2%, 4%, 8%) were (5.145, 4.86, 4.88, 4.95 **eV**), respectively. Furthermore, other optical parameters such as refractive index, extinction coefficient, and dielectric constant are studied.

Article Info

Keywords:
$\alpha - Al_2O_3$ nanoparticles , TEM, SAED, Optical band gap.

Article History:
Received: 19-June-2025,
Revised: 22-October-2025,
Accepted: 24-October-2025,
Available online: 28 December 2025.

1. INTRODUCTION

Nanotechnology deals with materials at the nano-scale level, where it studies matter in size $\leq$ 100 nanometer. The decrease in the size of materials provides many new physical and chemical properties, so there are many applications for these materials in different fields [1].

Alumina (Al_2O_3) is widely used in refractory, mechanical, abrasive, and insulator industries. Al_2O_3 is widely used as a catalyst in oxidation-reduction reactions because of its high surface area and thermal stability. Furthermore, alumina has good mechanical strength and a porous structure. The physical properties of materials mainly depend on their atomic configuration. Several alumina polymorphs exist and their oxygen atomic arrangements in close-packed structures can be divided into two crystal structure types: face-centered cubic (fcc) and hexagonal close-packed (hcp). Furthermore,

Al ions partially occupy the octahedral and/or tetrahedral interstices within the close-packed oxygen sublattice [2, 3]. α-Al_2O_3 (corundum) is a minor component of metamorphic rocks. However, only certain types of rocks that are richer in alumina and lower in silica can crystallize sapphire and ruby, two of its shining variations [4]. The direct band gap of α-Al_2O_3 in some literatures like, the bulk high-k insulator α-Al_2O_3 is 8.8 **eV** [5], α-Al_2O_3:Eu^{3+} nanophosphor is 5.7 **eV** [6], α-Al_2O_3:Dy^{3+} phosphor is 5.9 **eV** [7], α-Al_2O_3 nanoparticles is 5.25 **eV**, and 3.31 **eV** [8, 9].

This paper aims to study the morphology by transmission electron microscopy (TEM) and optical properties by UV-vis diffuse reflectance spectroscopy (UV-vis DRS) of (α-Al_2O_3):Zn nanoparticles prepared by the sol-gel technique to understand the electronic structure and optical features for exploring their effective use in optoelectronics.

2. MATERIALS AND METHODS

2.1. Materials

Aluminum nitrate nonahydrate ($Al(NO_3)_3$:$9H_2O$) (HIMEDIA,95%), zinc nitrate hexahydrate ($Zn(NO_3)_2$:$6H_2O$) (HIMEDIA, 99%), citric acid monohydrate ($C_6H_8O_7$.H_2O)

(HIMEDIA, 99%), and deionized water were obtained from Al-Shamel Chemical Industries (Sana'a).

2.2. Synthesis method

First, the flask was washed thoroughly with soap and water, then with ethanol, and then with distilled water. A molar ratio of 3:1 was used to dissolve 100 the aluminum nitrate nonahydrate ($Al(NO_3)_3{:}9H_2O$) (0.0899 **mol.**), 98% (0.088 **mol.**), 96% (0.08627 **mol.**), and 92% (0.0827 **mol.**) with citric acid monohydrate ($C_6H_8O_7.H_2O$) (0.0276 **mol.**) in 100 mL deionized water. The solution was then mixed with an appropriate amount of zinc nitrate hexahydrate ($Zn(NO_3)_2{:}6H_2O$) 2%(0.005 **mol.**), 4%(0.01 **mol.**), and 8%(0.02 **mol.**). The mixture was then swirled for 10 **min.** by using a magnetic stirrer. The mixture was then swirled for 2 **hrs** at 80 **℃** on the heated plate of the magnetic stirrer. After being heated to 100 **℃** for 30 min and allowed to cool to room temperature, a homogenous gel was created. The resulting dried powder was calcined for 2 h at 1100±10 **℃**.

2.3. Characterization

The morphology and nanoparticle size were determined using transmission electron microscopy (TEM) (JEM-2100, Japan) transmission electron microscope. ImageJ software was used to evaluate the particle size of the TEM. XRD analysis using a Pgeneral XD-2 X-ray diffractometer was performed for the prepared patterns (α-Al_2O_3):Zn in the range of $5° \leq 2\theta \leq 75°$. Diffuse reflectance was measured using (UV-vis DRS) (JASCO, V-750, Japan) over the wavelength range of $200 \leq \lambda \leq 2500$ **nm**.

3. RESULTS AND DISCUSSION

3.1. Morphology and XRD Study

3.1.1. TEM and SAED analysis

Transmission electron microscopy (TEM) is a suitable and useful method for assessing the morphology of nanoparticles, including the shape, size, growth, and distribution of crystallites [10]. The morphological results for the α-Al_2O_3:Zn patterns obtained from the TEM images are shown in Fig.1. This reveals that the clusters encompassing a large number of nanoparticles, as reported in Ref. [11] with regular and irregular spherical shapes of different sizes. The average particle sizes were (14.45, 9.52, 12.22 15.94 **nm**) for α-Al_2O_3:Zn (0%, 2%, 4%, and 8%) were 14.45, 9.52, and 12. The decrease in average particle size with increasing Zn concentration confirmed that Zn is a powerful reducing agent that controls the size of α-Al_2O_3 particles [12]. This result is in good agreement with that of a previous study [13]. Additionally, the TEM of the α-Al_2O_3:Zn nanoparticles showed little agglomeration growth. The literature in ref. [9] explained the agglomeration growth due to the continuous drying of the sol because the salts that remain in the sol form solid bridges between the particles as the water evaporates. Also, ref. [14] reported that the particles grow within the agglomerates owing to the spreading of ions at high temperatures.

The Selected Area Electron Diffraction (SAED) pattern shows concentric circular rings, indicating the polycrystalline nature of the α-Al_2O_3:Zn patterns shown in Fig.1.

The distribution histogram graphs of particle size and area of α-Al_2O_3:Zn patterns obtained using ImageJ software and Origin programs are shown in Fig.2. It can be seen that the diameters in the range (> 0 to 40, 18, 30 and 30 **nm)**, for α-Al_2O_3:Zn (0%, 2%, 4%, 8%) respectively.

3.1.2. XRD analysis

The XRD patterns of α-Al_2O_3:Zn nanoparticles are shown in Fig.3. The XRD pattern of pure α-Al_2O_3 emphasized its high crystallinity, and the diffraction peaks of the single-phase hexagonal structure matched well with (JCPDS file no. PDF#46-1212) with the space group R-3c (167) (corundum). This result agrees with previous works by Prashanth et al. and Farahmandjo M.et al. [8, 15]. The diffraction peaks of α-Al_2O_3:Zn (2%, 4%, and 8%) matched (file no. PDF#52-0803), (file no. 36-1451) and (file no. 4-831). The peak positions were slightly shifted towards higher angles as the Zn dopant concentration increased, owing to the substitution ionic radii between Zn^{2+} (0.74 **Å**) and Al^{3+} (0.57 **Å**) [16, 17]. The average crystallite size (D) was calculated using the Debye–Scherrer equation according to the following expression [18]:

$$D = 0.9\lambda / \beta \, cos\theta \tag{1}$$

λ (0.15406 **nm**) is the XRD wavelength of Cu-Kα, β is the full width at half maximum, and θ is Bragg's diffraction angle.

The Williamson–Smallman approach was used to calculate the dislocation density (δ) and measure the number of defects in the crystal using Eq. (2) [19]:

$$\delta = 1/D^2 \tag{2}$$

D is average of crystallite size.

The corresponding crystallite sizes and dislocation density values are summarized in Table 1. The degree of crystallite size reduction depends on the number of dopant-induced nucleation centers and the disruption of the growth stress caused by the different atomic radii of the Zn dopants and α-Al_2O_3, which is in good agreement with previous study [13].

The variation of crystallite size average and dislocation density with Zn concentration is shown in Fig.4.

Table 1. average D and δ of α-Al_2O_3:Zn nanoparticles

pattern	Average D (**nm**)	δx10^{-3} (**nm**)$^{-2}$	Lattice constants (**nm**)	
			a=b	c
Al_2O_3	30.529	1.15	0.4728	1.294
Al_2O_3:2%Zn	28.989	1.7	0.4726	1.287
Al_2O_3:4%Zn	27.51	1.93	0.4727	1.292
Al_2O_3:8%Zn	24.057	2.19	0.474	1.291

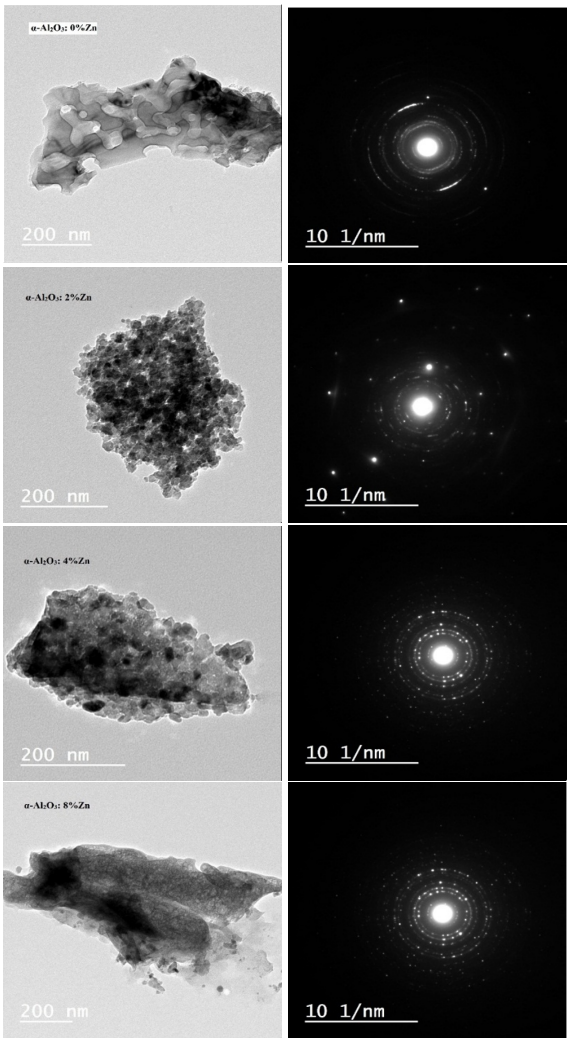

Figure 1. TEM And SEAD of α-Al_2O_3:Zn nanoparticles.

3.2. OPTICAL STUDY

The optical characterization and electronic interactions of the α-Al_2O_3:Zn nanoparticles were investigated.

3.2.1. Reflectance (R)

Fig. 5 shows that an enhancement in the reflectance spectra (R) is associated with a higher Zn (2%, 4%, especially 8%) content of α-Al_2O_3:Zn nanoparticles, indicating that enhancing its packing density [20], which decreases gradually at $\lambda < 520$ **nm** means more light is absorbed, which might be related to band gap or defect level changes. This suggests the possibility of using these materials as packaging materials. The altered reflectance near and beyond 1300 **nm** of Zn-doped α-Al_2O_3 reflects the presence and influence of Zn dopants and its impact on near-infrared absorption behavior, which may be attributed to the modification of the electronic structure of the α-Al_2O_3:Zn matrix.

3.2.2. Band gap energy

The band gap energy refers to the excitation of an electron from the top of the valence band to the bottom of the conduction band in optical absorption owing to the interaction of an electromagnetic wave with an electron in the valence band. This is a fundamental characteristic in the design of optoelectronic devices. The Kubelka-Munk expression is given by Eq. (3)[21, 22]

$$F(R) = (1-R)^2/2R \tag{3}$$

Where F(R) is the K-M function or remission corresponding to the absorbance, and R is the diffuse reflectance. The bandgap from Tauc's expression is given by Eq. (4) [23]

$$(F(R)\,h\upsilon) = A(h\upsilon - E_g)^n \tag{4}$$

F(R) is the K-M function, and A is the proportionality constant that describes the degree of material disorder, n=1/2, 3/2, 2, and 3 according to an inter-band transition type, that is, direct allowed and direct forbidden, indirect allowed, and indirect forbidden transitions, respectively. Plot of $(F(R)h\upsilon)^2$ versus incident photon energy $(h\upsilon)$. At the absorption edge on the X-axis at $(F(R)h\upsilon)^2 = 0$, the linear fit intercept gives the energy bandgap (E_g) [24]. Fig.6 shows $(F(R)h\upsilon)^2$ versus for the α-Al_2O_3:Zn samples. The reduction in the energy gap values of α-Al_2O_3:Zn (2%, 4%, and 8%) compared to the pure sample indicates that the Zn content enhances the ability of the materials to absorb photons, which is beneficial for generating reactive oxygen species (ROS) and, therefore, the photocatalytic process. This result is consistent with the results in Ref [25]. The creation of localized states inside the forbidden zone between the lowest empty molecular orbital and highest occupied molecular orbital explains this occurrence. Defects in the optical band gap could result from the dissolution of the bonds in Al_2O_3 owing to the presence of Zn. The energy of the highest occupied molecular orbital states implicitly increases the outcome of these defects in the creation of localized states. The concentration of defects is directly correlated with the density of the localized states. Moreover, the decrease in the bandgap value is caused by the appearance of empty levels induced by defects located in the bandgap. The defect concentration in materials affects their band gap, which is ascribed to the formation of localized states within the forbidden region, or linked to structural modification as in XRD analysis due to the interaction between Al_2O_3 and Zn ions. Different variables, such as variations in structural parameters such as grain size, lattice strain, and impurities, affect the change in

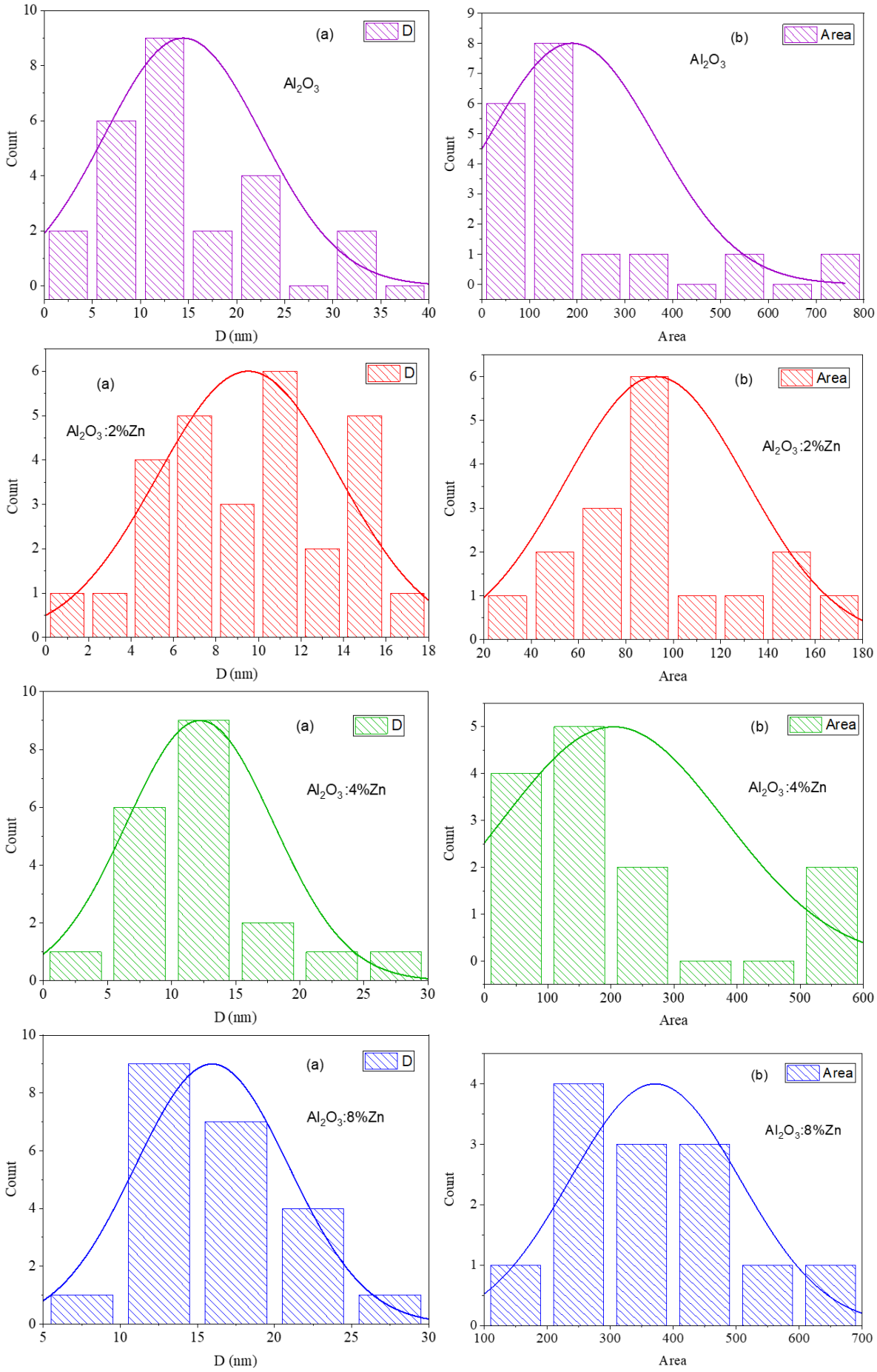

Figure 2. (a) The particle distribution (b) Area distribution of α-Al_2O_3:Zn nanoparticles.

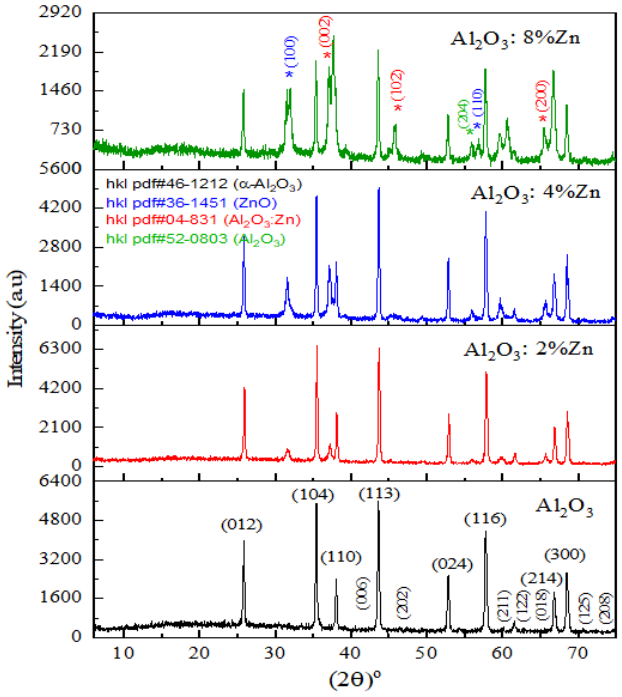

Figure 3. XRD patterns of α-Al_2O_3:Zn nanoparticles

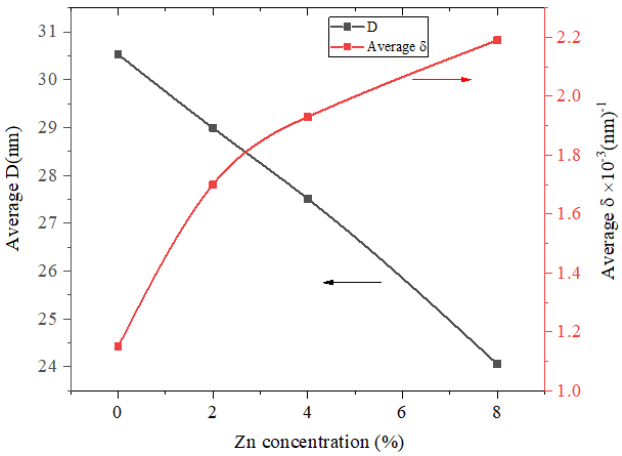

Figure 4. Variations of D and δ of α-Al_2O_3:Zn samples with Zn .

band gap [26, 27]. The energy levels in α-Al_2O_3 are produced above the valence band and below the conduction band by both the donor (oxygen vacancies) and acceptor defects (Al interstitials). The formation of energy levels is explained by the Frenkel reaction for Al interstitial defects and Schottky reactions for oxygen vacancy defects [28, 29]. The energy gaps of the prepared patterns are listed in Table.2. In the literature [30], the outcome of the energy gap of α-Al_2O_3 (5.28 eV).

3.2.3. Urbach energy

The Urbach energy (E_u) displays the strain fields and localized defect levels in the forbidden gap. In contrast, photon energy below the optical band gap causes optical transitions in the forbidden band gap. This was

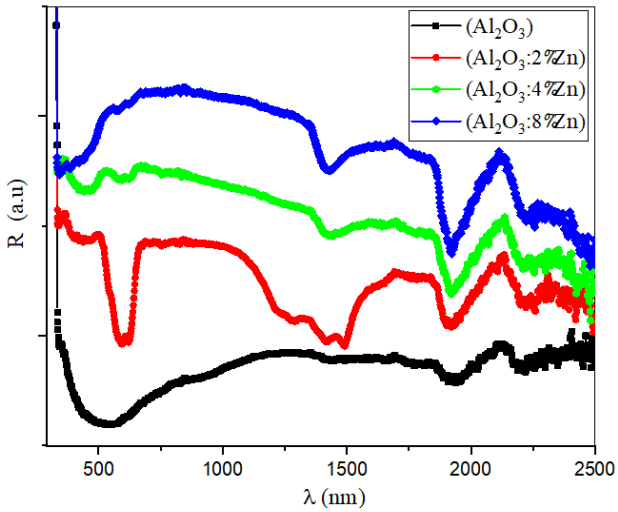

Figure 5. Diffuse reflectance spectra of α-Al_2O_3:Zn pattrens.

Table 2. The value of energy gap and Urbach energy

pattern	E_g (**eV**)	E_u (**eV**)
Al_2O_3	5.145	0.1514
Al_2O_3:2%Zn	4.86	0.1997
Al_2O_3:4%Zn	4.88	0.1084
Al_2O_3:8%Zn	4.95	0.1013

caused by electrical disorder (or localized tail states) in the forbidden band gap [31]. According to Pankove's expression, the absorption coefficient (α) exhibits exponential behavior in the low-energy range, as shown in Eq. (5) [32]:

$$\alpha = \alpha_{\circ}\exp(h\upsilon / E_u) \quad (5)$$

Fig.7 shows the linear fitting of a straight line of the curve of plot vs. , which gives the Urbach energy (Table 2).

Fig.8 illustrates the E_u and E_g as a function of the Zn% concentration. tends to decrease as the Zn concentration increases because of the decrease in the width of the localized states in the optical band [33]. This explains the variation in the disorder and defect contents depending on the Zn doping content. Furthermore, it exhibited the opposite behavior to the optical band gap. This indicates that the disorder variation causes a change in the optical bandgap.

3.2.4. Extinction coefficient (k)

The complex refractive index ($\hat{n} = n - ik$) was determined as the imaginary part (k (extinction coefficient)) and real part (n (refractive index)), according to Eq. (5) and Eq. (6) in the numerical section. The extinction coefficient (k) measured

amount of light lost by scattering and absorption in penetrating the material, that is, k provides the quantity of attenuation when the electromagnetic wave propa-

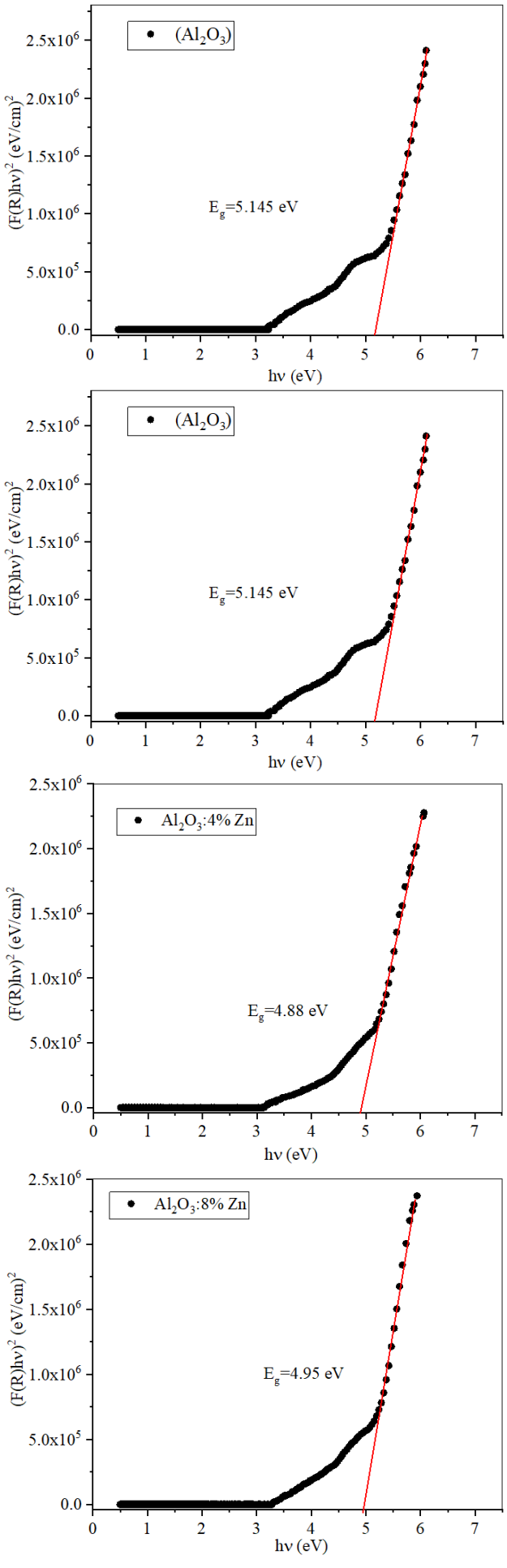

Figure 6. Energy gap of α-Al_2O_3:Zn nanoparticles

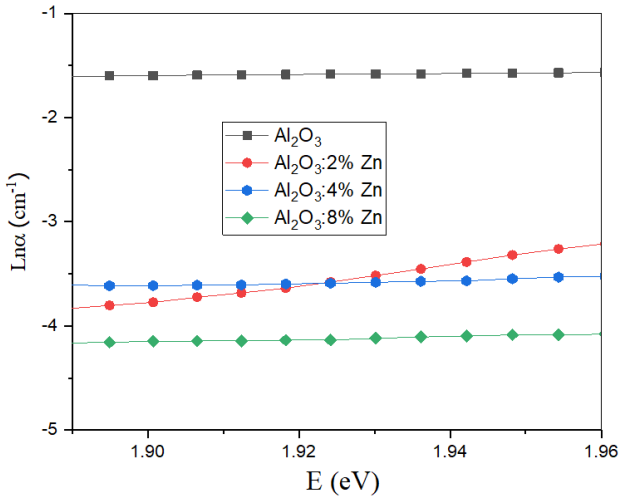

Figure 7. Urbach energy of α-Al_2O_3:Zn nanoparticles.

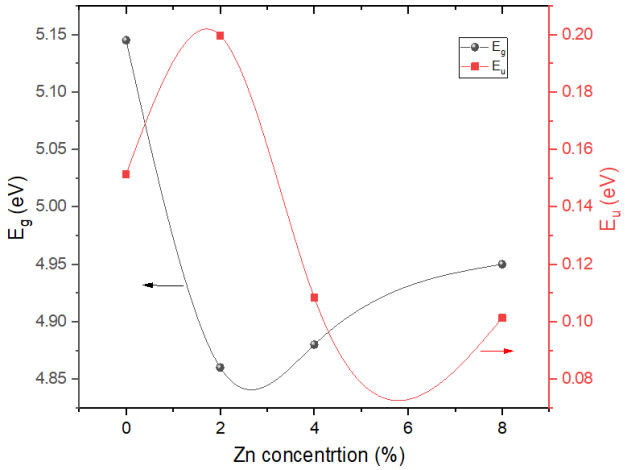

Figure 8. Variation of E_u and E_g with Zn concentration.

gates through the material and results in the loss of light propagation or light absorption through the material. It is expressed by Eq. (6) [34–36].

$$k = \alpha\lambda/4\pi \tag{6}$$

α is the absorption coefficient and λ is the wavelength.

Fig.9 shows the correlation between k and the incident photon energy ($h\upsilon$). It is evident that k decreases as the incident photon energy and Zn concentration increase, and the higher incident photon energy k tends to increase. This indicates that the fraction of light lost due to absorbance and scattering increases. In general, a small value of k reflects electromagnetic wave absorption owing to inelastic scattering processes [37, 38]. The ability to transition to another state is determined by the energy level, with a low k value indicating sufficient energy, and a high k value indicating insufficient energy for the electron to transition at this specific wavelength [39].

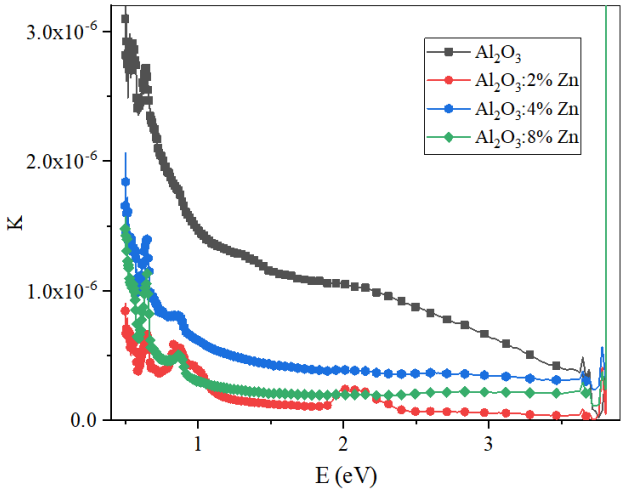

Figure 9. Extinction coefficient as a function of incident energy.

3.2.5. Refractive index (n)

The refractive index (n) indicates the relative velocity and refraction distribution of light through the material, and is related to the local fields and electronic polarization of ions into the material. The fabrication of optical devices depends on these devices. The refractive index can be estimated using Eq. (7) using reflectance [40, 41]:

$$n = \frac{1+R}{1-R} + \sqrt{\left(4R/(1-R)^2\right) - k^2} \tag{7}$$

R is a reflectance, k is the extinction coefficient.

The increase in the refractive index with increasing at low incident photon energies, as depicted in Fig. 10, is due to the absorption of energy, which leads to an increase in the effective electric susceptibility of the material. The reduction in the higher photon energy was due to the gradually implemented inner reflection or trapping of energy inside the grain boundaries [42]. Higher zinc concentrations tend to enhance the refractive index. This increase can be explained by the permittivity of the material, which can be linked to the polarization of Zn^{2+} [27]. This change in the refractive index indicates that doping modifies the optical properties of α-Al_2O_3 by increasing its ability to bend light.

3.2.6. Dielectric constants

The dielectric constants provide details on the permittivity and polarization capacity of a material. There is a real portion (ε_r) and an imaginary portion (ε_i). This is due to the concentration of the electronic polarization [36, 43].

The real part (ε_r) measures the ability of the material to slow down the light speed by grown nanocrystals, and is related to the refractive index using Eq. (8) [42, 44]

$$\varepsilon_r = n^2 - k^2 \tag{8}$$

n is refractive index, k is extinction coefficient.

Fig. 11 shows the variation ε_r vs. $h\upsilon$. Zn doping modifies the ε_r value, making it larger than that of pure α-Al_2O_3, indicating an enhanced polarization ability.

An imaginary portion (ε_i) is associated with the absorption of the material light. It represents the energy absorption from an electric field due to dipole motion, and is calculated using Eq. (9) [42, 44]

$$\varepsilon_i = 2nk \tag{9}$$

n is refractive index, k is extinction coefficient.

The imaginary part in Fig. 12 illustrates the relationship between ε_i and $h\upsilon$. A higher Zn content results in higher ε_i values, indicating stronger absorption due to the additional electronic transitions introduced by the Zn dopants. The opposite behaviors of ε_r and ε_i can be attributed to the effect of the Zn dopant. The small value of ε_i makes this material appropriate for optoelectronic devices [45]. For the grown nanoparticles, the highest absorption occurred at higher values of ε_r and ε_i [36].

3.2.7. Optical conductivity

The optical conductivity (σ_{opt}) can be utilized to investigate the optical response of the material to the spreading of charge carriers owing to the excitation caused by the photon energy of the event. It depends on the absorption coefficient and is calculated using Eq. (10) [46, 47].

$$\sigma_{opt} = \alpha nc/4\pi \tag{10}$$

c is the light velocity, α is absorption coefficient.

Fig.13 shows that the σ_{opt} increases as $h\upsilon$ increases and the growth starts at 3.8 **eV**, signifying the beginning of electronic transitions or absorptions that contribute to the material's optical response and the maximum growth around (5.8-6.1 **eV**), with an optical conductivity maximum value around $(5.5x10^{11} - 6.8x10^{11}\,\mathbf{s^{-1}})$ owing to

electrons excited by the photon energy. Higher Zn concentrations led to a more significant increase in optical conductivity. This suggests that Zn atoms introduce additional free charge carriers or energy states that enhance the response of the material to light, improving the doping of Al_2O_3 better at conducting under optical excitation. This is referred to as electron excitation from the valence band to the conduction band because light absorption leads to an increase in the absorption coefficient, making it an excellent material for optoelectronic devices [36, 48].

The two photoconductivity peaks were distributed at distinct wavelengths in the two zones. At a certain wavelength, this material appears to be absorbed more in the ultraviolet and visible spectrums [49].

3.2.8. Optical susceptibility

Optical susceptibility (χ_{opt}) describes the material response to an optical wavelength. Eq. (11) is calculated

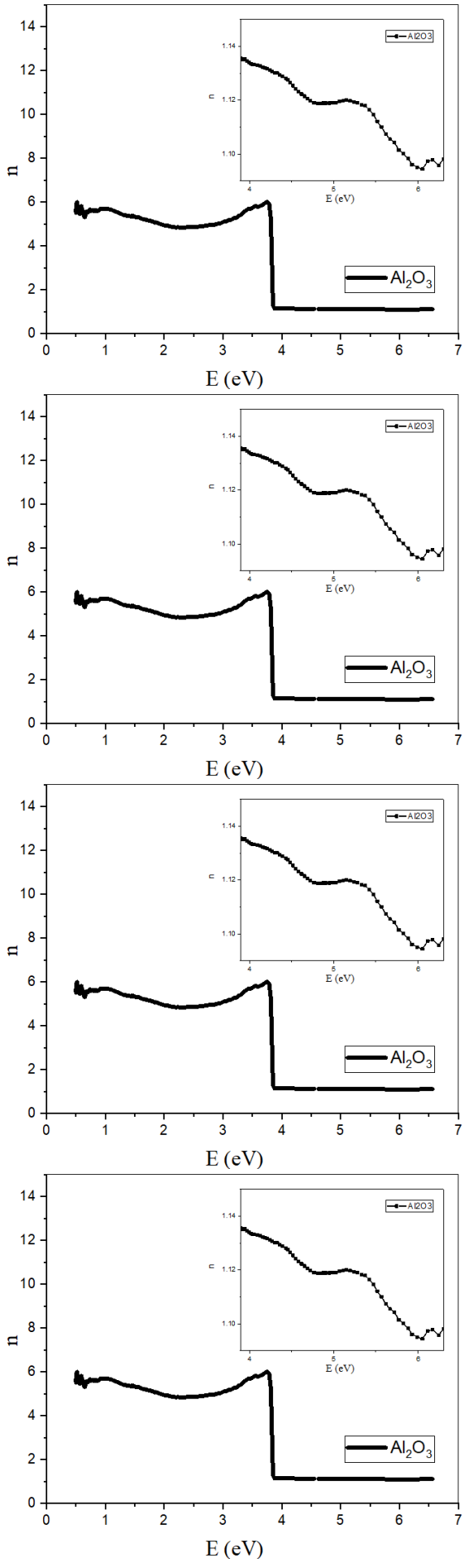

Figure 10. The refractive index with incident photon energy.

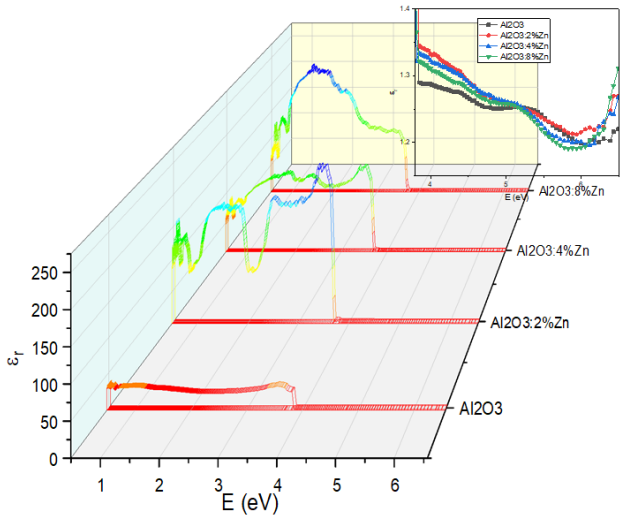

Figure 11. Variation of real part of the dielectric constant with incident photon energy.

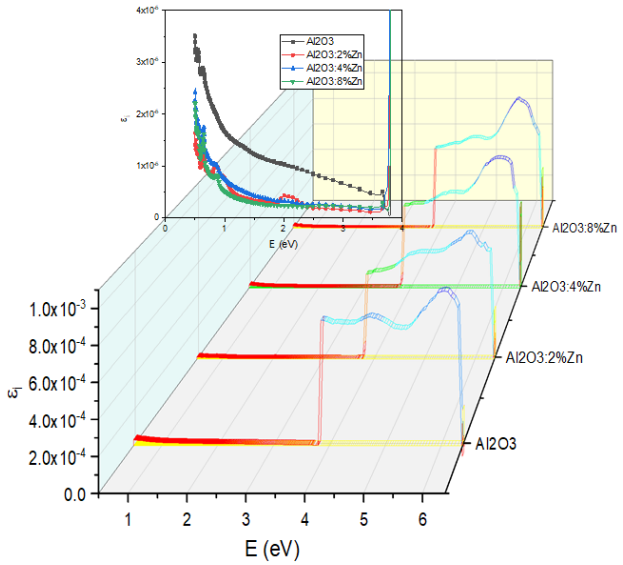

Figure 12. Variation of imaginary part of the dielectric constant with incident photon energy.

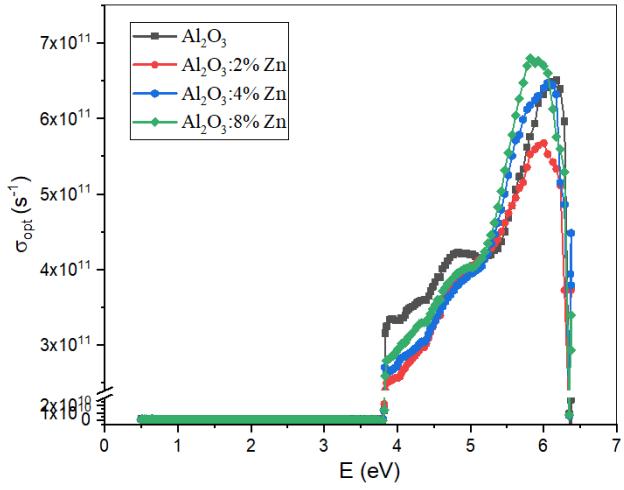

Figure 13. The corelation between σ_{opt} and photon energy.

as [50].

$$\chi_{opt} = (n^2 - 1)/4\pi \quad (11)$$

Zn doping alters the optical susceptibility of Al_2O_3, changing the shape and magnitude of its response to the photon energy, as shown in Fig. 14. This change implies that Zn doping modifies the electronic structure or polarizing ability of the material, possibly by introducing new electronic states or enhancing polarizable defects. Enhancement of optical susceptibility with a high Zn content. This suggests that adjusting the doping levels makes materials suitable in the domains of nonlinear optics and photonics.

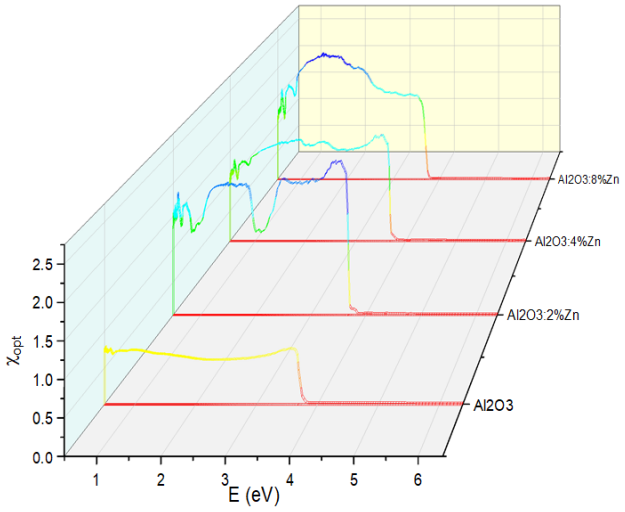

Figure 14. The optical susceptibility as function of photon energy.

4. CONCLUSION

In summary, (α-Al_2O_3):Zn nanoparticles were successfully prepared using the sol–gel method. TEM images showed the existence of regular and irregular spherical shapes and hexagonal structures at the nanoscale level. XRD confirmed the hexagonal structure with a polycrystalline structure, and the crystallite size of Zn-doped α-Al_2O_3 was smaller than that of the undoped α-Al_2O_3. The reflectance spectral features reflect the interaction between the α-Al_2O_3:Zn nanoparticles and light across the UV, visible, and NIR wavelengths. This tunability through Zn doping offers versatility in optimizing these materials for applications in UV protection, photocatalysis, optoelectronics, NIR devices, and sensing technologies. The values of the optical band gap of the α-Al_2O_3:Zn nanoparticles decreased as the Zn content increased, modified the electronic transitions, and introduced new energy states. The extinction coefficient, refractive index, and Zn dopant dependence on the incident photon energy make the material suitable for optical data storage device applications. The refractive index increased with increasing concentration of Zn ions. Adjusting the doping levels modifies ε_r and ε_i, enabling precise control over optical properties such as the refractive index and absorption characteristics, which are crucial for designing functional optical materials. The conductivity peaks indicated good photosensitivity.

REFERENCES

[1] I. Khan, K. Saeed, and I. Khan, "Nanoparticles: Properties, applications and toxicities," *Arab. J. Chem.*, vol. 12, no. 7, pp. 908–931, 2019. DOI: 10.1016/j.arabjc.2017.05.011.

[2] A. Noor, F. Afriani, R. A. Rafsanjani, and Y. Tiandho, "Characterization of aluminum oxide nanoparticles using egg white as a trap-matrix," *IOP Conf. Series: Earth Environ. Sci.*, vol. 353, p. 012 049, 2019. DOI: 10.1088/1755-1315/353/1/012049.

[3] S. Adachi, M. Ishimaru, Y. Sina, C. J. Mchargue, K. E. Sickafus, and E. Alves, "Corundum-to-spinel structural phase transformation in alumina," *Nucl. Instruments Methods Phys. Res. Sect. B*, vol. 358, pp. 136–141, 2015. DOI: 10.1016/j.nimb.2015.06.005.

[4] E. S. Sorokina, W. Hofmeister, T. Häger, R. Mertz-Kraus, S. Buhre, and J. M. Saul, "Morphological and chemical evolution of corundum (ruby and sapphire): Crystal ontogeny reconstructed by empa, la-icp-ms, and cr^{3+} raman mapping," *Am. Mineral.*, vol. 101, pp. 2716–2722, 2016. DOI: 10.2138/am-2016-5614.

[5] R. C. R. Santos, E. Longhinotti, V. N. Freire, R. B. Reimberg, and E. W. S. Caetano, "Elucidating the high-k insulator α-al_2o_3 direct/indirect energy band gap type through density functional theory computations," *Chem. Phys. Lett.*, vol. 637, pp. 172–176, 2015. DOI: 10.1016/j.cplett.2015.08.004.

[6] S. Kumar, R. Prakash, V. Kumar, G. M. Bhalerao, R. J. Choudhary, and D. M. Phase, "Surface and spectral studies of eu^{3+} doped α-al_2o_3 synthesized via solution combustion synthesis," *Adv. Powder Technol.*, vol. 26, no. 4, pp. 1263–1268, 2015. DOI: 10.1016/j.apt.2015.06.009.

[7] S. Kumar, R. Prakash, and V. Kumar, "A novel yellowish white dy^{3+} activated α-al_2o_3 phosphor: Photoluminescence and optical studies," *Funct. Mater. Lett.*, vol. 8, no. 5, p. 1 550 061, 2015. DOI: 10.1142/S1793604715500617.

[8] P. A. Prashanth, R. S. Raveendra, R. Hari Krishna, et al., "Synthesis, characterizations, antibacterial and photoluminescence studies of solution combustion-derived α-al_2o_3 nanoparticles," *J. Asian Ceram. Soc.*, vol. 3, no. 3, pp. 345–351, 2015. DOI: 10.1016/j.jascer.2015.07.001.

[9] V. P. Dhawale, D. J. Late, and S. D. Kulkarni, "Synthesis, characterization of α-al_2o_3 nanoparticles and its application in decolorization of methyl orange azo dye in the presence of uv light," *J. Nanosci. Technol.*, vol. 5, no. 1, pp. 580–583, 2019.

[10] S. Taha, M. Ezzeldien, K. H. Omran, and M. S. A. El-sadek, "$Zn_{1-x}mg_xo$ nanocomposites: Synthesis, structural, optical properties and antibacterial activity," *Egypt. J. Phys.*, vol. 51, pp. 35–56, 2023. DOI: 10.21608/EJPHYSICS.2022.157498.1085.

[11] A. A. Mohammed, Z. T. Khodair, and A. A. Khadom, "Preparation and investigation of the structural properties of α-al_2o_3 nanoparticles using the sol-gel method," *Chem. Data Collect.*, vol. 29, p. 100 531, 2020. DOI: 10.1016/j.cdc.2020.100531.

[12] A. A. S. Ahmed, A. A. A. Al-mushki, B. A. Al-asbahi, H. M. Ghaithan, W. A. Farooq, and H. Omar A. El Kader, "Effect of ethylene glycol concentration on the structural and optical properties of multimetal oxide cdo–nio–fe_2o_3 nanocomposites for antibacterial activity," *J. Phys. Chem. Solids*, vol. 155, p. 110 113, 2021. DOI: 10.1016/j.jpcs.2021.110113.

[13] C. Ragupathi, S. Narayanan, P. Tamizhdurai, T. A. Sukantha, and G. Ramalingam, "Correlation between the particle size, structural and photoluminescence spectra of nano $nicr_2o_4$ and la-doped $nicr_2o_4$ materials," *Heliyon*, vol. 9, no. 11, e21981, 2023. DOI: 10.1016/j.heliyon.2023.e21981.

[14] D. G. Syarif, D. H. Prajitno, and J. S. Pane, "Effect of calcination temperature during synthesis of al_2o_3 from local bauxite on stability and chf of water–al_2o_3 nanofluids," *J. Aust. Ceram. Soc.*, 2017, Published online. DOI: 10.1007/s41779-017-0125-8.

[15] M. Farahmandjou and N. Golabiyan, "New pore structure of nano-alumina (al_2o_3) prepared by sol gel method," *J. Ceram. Process. Res.*, vol. 16, no. 2, pp. 1–4, 2015.

[16] L. Sinusaite, A. Popov, A. Antuzevics, et al., "Fe and zn co-substituted beta-tricalcium phosphate (β-tcp): Synthesis, structural, magnetic, mechanical and biological properties," *Mater. Sci. Eng. C*, vol. 128, p. 110 918, 2021. DOI: 10.1016/j.msec.2020.110918.

[17] H. Sun, P. Li, S. Yan, and G. Wang, "Effects of al_2o_3 species and particle sizes on properties of al_2o_3–cr_2o_3 refractories," *Mater. Sci. Forum*, vol. 745–746, pp. 610–615, 2013. DOI: 10.4028/www.scientific.net/MSF.745-746.610.

[18] S. A. J. Jassim and E. M. Ali Nassar, "Effect of deposition time on the structure, direct and indirect energy gap of nanoparticles cdo thin films deposited by chemical bath deposition technique," *J. Physics: Conf. Ser.*, vol. 1879, no. 3, p. 032 106, 2021. DOI: 10.1088/1742-6596/1879/3/032106.

[19] S. A. J. Jassim and E. M. A. Nassar, "Effect of annealing temperature on structure and optical properties of cdo nanocrystalline thin film prepared by chemical bath deposition method," *IOP Conf. Series: Mater. Sci. Eng.*, vol. 928, no. 7, p. 072 046, 2020. DOI: 10.1088/1757-899X/928/7/072046.

[20] A. A. Al-Muntaser, E. Alzahrani, A. Saeed, et al., "Exploring the influence of sudan iv azo dye on the structural, optical, and dispersion characteristics of pva/su-iv composites," *Phys. Scripta*, vol. 99, p. 105 991, 2024.

[21] N. Sharma, K. Prabakar, S. Ilango, S. Dash, and A. K. Tyagi, "Optical band-gap and associated urbach energy tails in defected aln thin films grown by ion beam sputter deposition: Effect of assisted ion energy," *Adv. Mater. Proc.*, vol. 2, no. 5, pp. 342–346, 2017. DOI: 10.5185/amp.2017/511.

[22] S. N. Aziz, A. M. Abdulwahab, and T. S. Aldeen, "Synthesis and characterization of (cdo–cuo–co_3o_4) mixed metal oxides nanocomposite," *Sana'a Univ. J. Appl. Sci. Technol.*, vol. 2, no. 2, pp. 116–123, 2024.

[23] K. Saravanakumar and S. Muthupoongodi, "A novel n-ceo_2/n-cdo heterojunction nanocomposite for enhanced photodegradation of organic pollutants under visible light irradiation," *J. Rare Earths*, vol. 37, no. 8, pp. 853–860, 2019. DOI: 10.1016/j.jre.2018.12.009.

[24] R. J. Stella, G. T. Rao, V. P. Manjari, B. Babu, C. Rama, and R. V. S. S. N. Ravikumar, "Structural and optical properties of cdo/zns core/shell nanocomposites," *J. Alloy. Compd.*, vol. 628, pp. 39–45, 2015. DOI: 10.1016/j.jallcom.2014.11.201.

[25] K. Portillo-Cortez, U. Caudillo-Flores, S. Perla, E. Smolentseva, S. Fuentes-Moyado, and D. Dominguez, "Photocatalytic activity of ag nanoparticles deposited on thermoexfoliated g-c_3n_4," *Nanomaterials*, vol. 14, no. 7, p. 623, 2024. DOI: 10.3390/nano14070623.

[26] S. Aydemir, S. Köse, M. S. Kilickaya, and V. Özkan, "Influence of al-doping on microstructure and optical properties of sol-gel derived cdo thin films," *Superlattices Microstruct.*, vol. 71, pp. 72–81, 2014. DOI: 10.1016/j.spmi.2014.03.010.

[27] S. A. Al Hashedi, A. M. A. El-Latif, A. A. Al-Muntaser, N. S. Al-Zoreky, K. M. A. Ramadan, and A. Q. Alosabi, "Effect of disodium phthalocyanine on the structural, optical, electrical, and dielectric properties of pva/cmc blend towards optoelectronic applications," *Int. J. Biol. Macromol.*, vol. 307, p. 141 840, 2025. DOI: 10.1016/j.ijbiomac.2025.141840.

[28] S. Usharani and V. Rajendran, "Size controlled synthesis and characterization of v_2o_5/al_2o_3 nanocomposites," *Colloids Interface Sci. Commun.*, vol. 24, pp. 7–12, 2018. DOI: 10.1016/j.colcom.2018.03.001.

[29] N. S. Bajaj and S. K. Omanwar, "Low-temperature stearic acid sol–gel synthesis of α-al_2o_3 quantum dots and its optical properties," *J. Sol-Gel Sci. Technol.*, vol. 75, pp. 1–5, 2015. DOI: 10.1007/s10971-015-3667-7.

[30] M. A. A. Al-Mushaki, S. A. Al-Ariki, and A. Alnehia, "Effect of copper oxide (cuo) and vanadium oxide (v_2o_5) addition on the structural, optical and electrical properties of corundum (α-al_2o_3)," *Sci. Reports*, vol. 13, no. 1, pp. 1–10, 2023. DOI: 10.1038/s41598-023-43309-1.

[31] A. Abdullah Ahmed Ali, A. M. Abdulwahab, Z. Abidin, D. Salah, and M. Hussein, "Magnetic and optical properties of synthesized zno–$znfe_2o_4$ nanocomposites via calcined zn–fe layered double hydroxide," *Opt. Mater.*, vol. 108, p. 110 179, 2020. DOI: 10.1016/j.optmat.2020.110179.

[32] S. Köse, F. Atay, V. Bilgin, and I. Akyüz, "In-doped cdo films: Electrical, optical, structural and surface properties," *Int. J. Hydrog. Energy*, vol. 34, no. 12, pp. 5260–5266, 2009. DOI: 10.1016/j.ijhydene.2008.11.110.

[33] A. H. A. Sakr, "Significance of lanthanum doping on physical, optical, magnetic, and dielectric properties of $coal_{2-x}la_xo_4$ nanoparticles," *Egypt. J. Phys. Sci.*, vol. 48, pp. 53–67, 2020.

[34] A. A. Al-Muntaser, M. M. El-Nahass, and H. A. Saad, "Dft calculation and experimental study on electronic structure and optical properties of 7-amino-4-oxo-3-(2-(2-thienyl)vinyl)-4h,8h-," *Optik*, vol. 220, p. 165 199, 2020. DOI: 10.1016/j.ijleo.2020.165199.

[35] B. Chacko, A. Roy, A. Melbin Richard, J. Swathy, B. T. Avanish, and W. Madhuri, "Bismuth modified zinc ferrites for low-temperature ceramic co-firing technology," *Mater. Chem. Phys.*, vol. 276, p. 125 401, 2022. DOI: 10.1016/j.matchemphys.2021.125401.

[36] S. Yasmeen, T. Munawar, M. Asghar, M. A. Khan, A. Hussain, and F. Iqbal, "Synthesis and photocatalytic study of $zn_{0.90}co_{0.10}o$ and $zn_{0.90}co_{0.05}m_{0.05}o$ (m = ca, ba, cr, pb) nanocrystals: Structural, optical and electrical investigations," *J. Mater. Res. Technol.*, vol. 9, no. 3, pp. 4076–4096, 2020. DOI: 10.1016/j.jmrt.2020.02.034.

[37] M. A. Ditta, M. A. Farrukh, S. Ali, and N. Younas, "X-ray peak profiling, optical parameters and catalytic properties of pure and cds-doped zno–nio nanocomposites," *Russ. J. Appl. Chem.*, vol. 90, no. 1, pp. 151–159, 2017. DOI: 10.1134/S1070427217010220.

[38] A. S. Varpe and M. D. Deshpande, "Structural and optical characteristics of ce-, nd-, gd-, and dy-doped al_2o_3 thin films," *Pramana – J. Phys.*, vol. 89, no. 1, pp. 1–11, 2017. DOI: 10.1007/s12043-017-1396-x.

[39] A. A. Al-Muntaser, S. A. Al-Ghamdi, E. Alzahrani, A. R. G. M. Asnag, and A. M. Al-Harthi, "Investigation of structural and optical characteristics of pva/crystal violet dye composites for flexible smart optoelectronic applications," *J. Polym. Res.*, vol. 31, p. 311, 2024. DOI: 10.1007/s10965-024-04160-8.

[40] N. Nazari, M. M. Golzan, and K. Mabhouti, "Study of urbach energy and kramers–kronig relations on mn- and zn-doped $nife_2o_4$ ferrite nanopowder for the determination of structural and optical characteristics," *Sci. Reports*, vol. 14, no. 1, pp. 1–23, 2024. DOI: 10.1038/s41598-024-57045-7.

[41] A. A. Al-Muntaser, E. Alzahrani, S. A. Al-Ghamdi, A. M. Al-Harthi, S. Aldwais, and A. Saeed, "Linear and nonlinear optical characteristics of basic fuchsin-doped polyvinyl alcohol films for flexible optoelectronics," *ECS J. Solid State Sci. Technol.*, vol. 13, no. 12, p. 124 001, 2024. DOI: 10.1149/2162-8777/ad9a79.

[42] M. F. Rahman, J. Hossain, and M. I. A. B., "Structural, surface morphological and optical properties and their correlation with the thickness of spin-coated cds thin films synthesized using a novel chemical route," *SN Appl. Sci.*, vol. 2, p. 1956, 2020. DOI: 10.1007/s42452-020-03836-2.

[43] O. Bawazeer, "Structural, optical, and shielding properties of lead borate glasses doped with copper oxide," *Mater. Res. Express*, vol. 11, no. 1, pp. 1–20, 2024. DOI: 10.1088/2053-1591/ad19b2.

[44] P. S. Rohith, N. Jagannatha, and K. V. P. Kumar, "Thermal, optical and electrical susceptibility studies of pure and calcium-doped nickel cadmium oxalate crystals," *Bull. Mater. Sci.*, vol. 44, no. 3, pp. 1–8, 2021. DOI: 10.1007/s12034-021-02486-3.

[45] V. Ganesh, L. Haritha, H. E. Ali, A. M. Aboraia, Y. Khairy, and H. H. Hegazy, "Detailed calculations of optical properties of indium-doped cdo nanostructured films using kramers–kronig relations," *J. Non-Crystalline Solids*, vol. 552, p. 120 454, 2021. DOI: 10.1016/j.jnoncrysol.2020.120454.

[46] A. Gültekin, G. Karan, F. Özel, M. Kus, and R. Say, "Synthesis and characterisation of au-nanoparticle-doped tio_2 and cdo thin films," *J. Phys. Chem. Solids*, vol. 75, pp. 775–781, 2014. DOI: 10.1016/j.jpcs.2014.01.011.

[47] T. S. Soliman and S. A. Vshivkov, "Effect of fe nanoparticles on the structure and optical properties of polyvinyl alcohol nanocomposite films," *J. Non-Crystalline Solids*, vol. 519, p. 119 452, 2019. DOI: 10.1016/j.jnoncrysol.2019.05.028.

[48] M. I. Fathima, A. M. S. Arulanantham, and K. S. J. Wilson, "Effect of zns nanowire arc on czts/cds thin film solar cells by nebulizer spray pyrolysis technique," *Mater. Res. Express*, vol. 7, p. 015 510, 2020. DOI: 10.1088/2053-1591/ab63f9.

[49] A. H. Al-Hammadi and S. H. Khoreem, "Investigations on optical and electrical conductivity of ba/ni/zn/$fe_{16}o_{27}$ ferrite nanoparticles," *Biointerface Res. Appl. Chem.*, vol. 13, no. 2, 2023. DOI: 10.33263/BRIAC132.168.

[50] S. A. Gad and A. A. Moez, "Enhanced optical conductivity, nonlinear optical and semiconducting properties of $mg_{1-x}cu_xo$/pmma nanocomposite," *J. Inorg. Organomet. Polym. Mater.*, vol. 30, pp. 469–476, 2020. DOI: 10.1007/s10904-019-01205-0.